Article

A Novel Dual Air-Bearing Fixed-χ Diffractometer for Small-Molecule Single-Crystal X-ray Diffraction on Beamline I19 at Diamond Light Source

David R. Allan [1],*, Harriott Nowell [1], Sarah A. Barnett [1], Mark R. Warren [1], Adrian Wilcox [1], Jeppe Christensen [1], Lucy K. Saunders [1] , Andrew Peach [1], Mark T. Hooper [1], Ljubo Zaja [1], Suren Patel [1], Leo Cahill [1], Russell Marshall [1], Steven Trimnell [1], Andrew J. Foster [1], Trevor Bates [1], Simon Lay [1], Mark A. Williams [1] , Paul V. Hathaway [1], Graeme Winter [1], Markus Gerstel [1] and Ron W. Wooley [2]

[1] Diamond Light Source, Harwell Campus, Chilton, Oxfordshire OX11 0DE, UK; Harriott.Nowell@diamond.ac.uk (H.N.); Sarah.Barnett@diamond.ac.uk (S.A.B.); Mark.Warren@diamond.ac.uk (M.R.W.); Adrian.Wilcox@diamond.ac.uk (A.W.); Jeppe.Christensen@diamond.ac.uk (J.C.); Lucy.Saunders@diamond.ac.uk (L.K.S.); Andrew.Peach@diamond.ac.uk (A.P.); Mark.Hooper@diamond.ac.uk (M.T.H.); Ljubo.Zaja@diamond.ac.uk (L.Z.); Suren.Patel@diamond.ac.uk (S.P.); Leo.Cahill@diamond.ac.uk (L.C.); Russell.Marshall@diamond.ac.uk (R.M.); Steven.Trimnell@diamond.ac.uk (S.T.); Andrew.Foster@diamond.ac.uk (A.J.F.); Trevor.Bates@diamond.ac.uk (T.B.); Simon.Lay@diamond.ac.uk (S.L.); Mark.Williams@diamond.ac.uk (M.A.W.); Paul.Hathaway@diamond.ac.uk (P.V.H.); Graeme.Winter@diamond.ac.uk (G.W.); Markus.Gerstel@diamond.ac.uk (M.G.)

[2] Fluid Film Devices Ltd., Unit 8, Greatbridge Business Park, Budds Lane, Romsey, Hampshire SO51 0HA, UK; ron.wooley1@virginmedia.com

* Correspondence: David.Allan@diamond.ac.uk; Tel.: +44-1235-778644

Abstract: Herein, we describe the development of a novel dual air-bearing fixed-χ diffractometer for beamline I19 at Diamond Light Source. The diffractometer is designed to facilitate the rapid data collections possible with a Dectris Pilatus 2M pixel-array photon-counting detector, while allowing remote operation in conjunction with a robotic sample changer. The sphere-of-confusion is made as small as practicably possible, through the use of air-bearings for both the ω and φ axes. The design and construction of the new instrument is described in detail and an accompanying paper by Johnson et al. (also in this issue) will provide a user perspective of its operation.

1. Introduction and Background

Small-molecule single-crystal diffraction techniques have evolved rapidly since the late 1960s. Data collection has advanced from laborious (and extremely time-consuming) film-based techniques, through the use of computer-automated serial detector-based diffractometers, to modern diffraction systems based on CCD detectors. With the parallel development of smaller and faster computing hardware, and advances in data collection, integration, structure solution and refinement software packages, a routine small-molecule crystal structure can be determined within a few hours rather than over the several months required for film-based methodologies. It is not unusual, therefore, for a well-equipped chemical crystallography laboratory to determine several hundred small-molecule crystal structures in a year [1].

Many of the advances in small-molecule crystallography have shared developments with macromolecular crystallography (MX), where there has been a move away from using CCD detectors to large-area pixel-array photon-counting detectors with their accompanying rapid frame rates and image read-out times. As these detectors can dispense with the timing shutter and step-scan mode (where a series of discrete oscillation images are taken) required for the integrating CCD detector, they can collect data in a "shutterless" mode where the goniometer can be slewed at a constant rotation speed while the detector collects diffraction images. The near elimination of time overhead between images allows data to be collected extremely efficiently at synchrotron sources, with comparable data sets being collected in a few seconds rather than several minutes. A typical macromolecular crystallography beamline, with an automated robotic sample changer, can collect data on potentially hundreds of crystals per day rather than the tens of samples possible just 5 years ago.

More recently, data collection in shutterless-mode has been implemented for small-molecule crystallography with the use of small format pixel-array detectors, such as the Dectris Pilatus 300 K detector [2], or specialised CMOS based integrating detectors, such as the Bruker Photon 100 detector [3]. Although the time overhead (due to detector read-out and goniometer slewing for step-scans) is less significant for a laboratory-based diffractometer, the time savings can, nevertheless, be appreciable. As well as the time savings, the increased sensitivity and lower inherent noise of the detector lead to an improvement in data quality, which is further enhanced by the reduction in error caused by any inaccuracy of the goniometer stepping motion or any jitter in the time for the shutter to either open or close.

Beamline I19, the high-flux tunable-wavelength facility for small-molecule crystallography at Diamond Light Source, UK, has been operational since September 2008. This was just before pixel-array photon counting detectors, such as the Dectris Pilatus, were widely adopted in macromolecular crystallography [4–6]. The beamline has two experiments hutches with experiments hutch 1 (EH1) providing a high-throughput diffractometer for chemical crystallography studies. Experiments hutch 2 (EH2) offers a heavy-duty diffractometer for experiments requiring bulky sample environment equipment, such as a cryostat, or for experiments requiring a complex set up, such as time-resolved pump-probe studies using a pulsed laser. Both diffractometers were initially fitted with CCD detectors but, after approximately two years of operation, the large Newport four-circle diffractometer housed in EH2 was equipped a Pilatus 300 K detector; the first of its type and manufactured as a prototype by Dectris especially for I19. The introduction of the Pilatus 300 K detector transformed the capabilities of the diffractometer, greatly increasing the speed of data collections. The detector's high frame rate and the use of high-frequency gating of its photon counting discriminator also give it unique capabilities for time-resolved studies.

When the beamline became operational, EH1 housed a 4-circle κ-geometry diffractometer manufactured by Crystal Logic, which was integrated by Rigaku with their Saturn 724+ CCD detector and ACTOR robotic sample changer. Rigaku also incorporated an Oceaneering 3-axis "microglide" motorised goniometer head to allow crystals to be centred on the diffractometer remotely once they had been mounted, or exchanged, by the robot. The diffractometer and robot were controlled by the Windows software, CrystalClear and CameraMan respectively, provided by Rigaku (CrystalClear-SM Expert 2.0 r5 Rigaku America, The Woodlands, TX, USA) [7]. This turn-key system initially proved to be the workhorse of the beamline and, with the microglide removed, it could be adapted for high-pressure studies employing diamond-anvil cells, or for studies of gas-exchange in porous crystalline materials using gas environment cells. However, with the development of the Pilatus 300 K detector in EH2 providing dramatically improved data collection efficiency, all sample environment studies were migrated to EH2 leaving EH1 to support structural determinations exclusively. At this juncture, the requirements for the EH1 diffractometer were reappraised in light of over 8 years of user operation and experience. A project was instigated to upgrade the diffractometer so that its capabilities could be optimised for structural determination studies and to fully exploit the new opportunities offered

by photon-counting pixel-array detectors. The unrivaled mechanical precision of air-bearings was exploited for both the ω and φ axes to minimise the sphere-of-confusion.

2. Diffractometer Description and Key Principles

The fully focused beam at the sample position in EH1 is in the order of 50 μm in the vertical and 80 μm in the horizontal (FWHM), with the current focusing optics. Therefore, a goniometer with a sphere-of-confusion of 10 μm or less is needed to ensure that sample crystals remain well aligned to the beam. This requirement is difficult to realise with a vertically oriented diffractometer (which is necessary due to the polarisation of the synchrotron X-ray beam) as the load on the goniometer components will vary substantially as the axes reorient relative to gravity. The original 4-circle κ-diffractometer had a sphere-of-confusion somewhat larger than this tolerance (approximately 25 μm) and, therefore, a degree of beam defocussing was necessary to accommodate drifts in the sample position as the goniometer axes (ω, κ and φ) were rotated. A goniometer with much improved mechanical stability was required to allow micron-sized crystals to be studied with a fully optimised beam. Not only would the main goniometer need to be suitably stable, but all components in the long mechanical chain from the sample mount through to the diffractometer table would also need to be equally stiff. This places particularly stringent demands on the 3-axis (x,y,z) sample stage which would need to maintain positional stability, both in slip and sag, over a variety of orientations.

To improve the likelihood of developing a multi-axis goniometer with the required mechanical stability, a fixed-χ geometry (with χ set to the magic angle of 54.74°) was adopted for the design which dispenses with the complexities of a κ-instrument. Although this loses some of the orientational flexibility offered by a κ-goniometer, the fixed-χ geometry (which is familiar to most chemical crystallographers due to the popular Bruker D8 diffractometer) does provide sufficient access to reciprocal space such that complete and redundant data sets can be harvested for all crystal systems [8,9]. The fixed-χ design allows the mechanical alignment of the φ-axis onto the ω-axis to be carried out extremely easily and, as the geometry does not change, it can maintain balance throughout a complete rotation of ω (unlike a vertically mounted κ-goniometer which can only achieve balance at a single κ-angle). As the goniometer can be accurately balanced this further enhances stability and also, crucially, allows the speed of rotation to be maintained very accurately throughout a scan. Additionally, as the fixed-χ goniometer has a relatively open geometry, use of a carefully designed beam collimator, beamstop and sample viewing camera, means only collisions with the detector need to be avoided in the controls software thereby removing the need for complex collision modelling.

In order to achieve the best possible mechanical reproducibility, a novel dual air-bearing design for the fixed-χ goniometer was adopted. Air-bearings are now used routinely for high-precision rotary stages, and are used exclusively for the single-axis goniometers on all the MX beamlines at Diamond, as they offer sub-micron runout errors in their motion which cannot be matched by conventional mechanical bearings suitable for goniometry. For the fixed-χ goniometer described here, both the ω-axis and the φ-axis incorporate air-bearings to provide the best possible rotational accuracy. The design incorporates slip-rings for both the compressed-air and electrical supplies so that both ω and φ can be rotated an unlimited number of times without the wrapping of cables or tubing. This is an important consideration as any slight angle-dependent strain applied to the goniometer from twisting cables or tubes could affect the overall alignment of the instrument.

The goniometer, as shown in Figure 1, is mounted within a vertically oriented Huber circle that holds the 2θ arm for the detector. The detector, a Pilatus 2M, is mounted via a translation stage that enables the sample to detector distance to be varied. The Pilatus 2M allows a comparatively large sample to detector distance while still capturing a sufficiently large volume of reciprocal space (to an appropriately high resolution for publication of the structure at the "standard" I19 wavelength of 0.6889 Å) at one detector setting. The larger sample to detector distance is a crucial element in reducing the background from air-scatter to collect the best possible data sets from the most weakly

scattering crystals (which proved to be a serious limitation for the small CCD detector of the previous EH1 diffractometer).
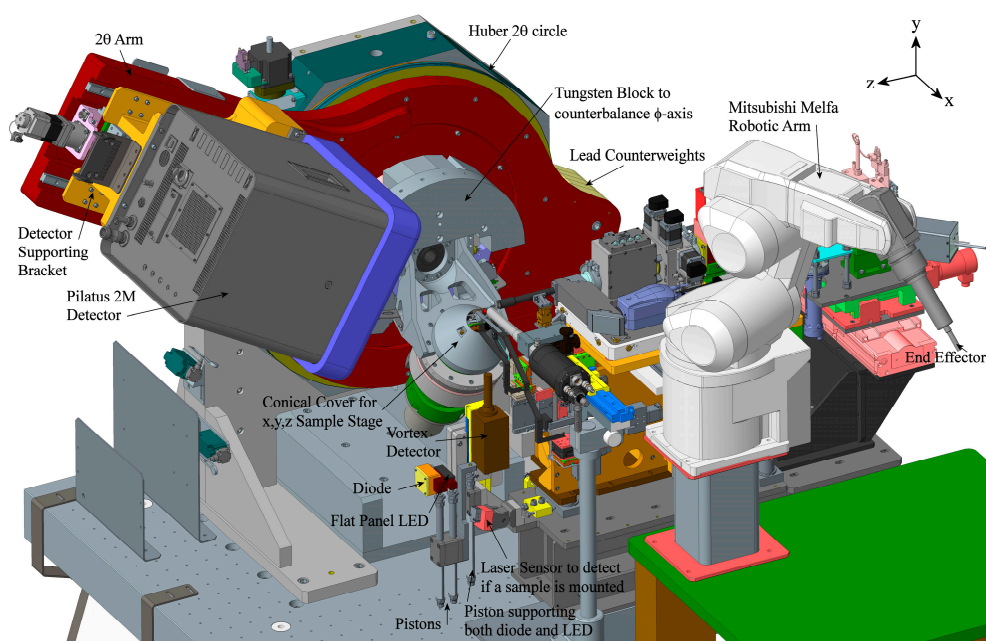

Figure 1. A general view of the complete end-station. The Dewar and the sample trays have been omitted for clarity. The indicated coordinate system is from the Diamond Light Source engineering standards and is used to define the sense of travel of the linear stages. The rotary stages of the diffractometer move in a positive sense when they are rotated clockwise as viewed from the front of the instrument. The diffractometer is depicted with $2\theta = 30°$, $\omega = 0°$, $\varphi = 0°$ and with a detector distance of 500 mm (i.e., the distance between the detector sensor chips and the sample position).

The sample viewing camera, beam collimation, fast shutter and beamstop assemblies are housed within a frame mounted to the jacking table at the front of the diffractometer. The design borrowed many of its key features from the MX beamlines at Diamond. The sample viewing camera, or on-axis viewer (OAV), has a periscopic arrangement whereby the objective lens and first mirror in the optical path have holes to allow the beam to pass through to the sample. This arrangement permits the user to view the sample as the X-rays would "see" it and has the additional advantage of allowing the beam to be aligned to the goniometer centre more easily with the aid of a retractable fluorescent screen.

2.1. The Dual Air-Bearing Fixed-χ Goniometer

Perhaps the most novel element of the entire instrument is the dual air-bearing fixed-χ goniometer which, to the best of our knowledge, is the first of its type to be built. The air-bearings, and associated air slip-ring, were designed and manufactured by Fluid Film Devices Ltd., Romsey UK, from an initial set of concept drawings.

Some highly bespoke mechanical bearings (such as those composed of spindles incorporating angular contact ball bearings of the ABEC 9 quality [10]) can achieve a non-repeatable runout within ± 0.25 µm. Although these bearings are often used in highly specialised applications such as within gyroscopes for inertial navigation systems, they are susceptible to wear. The issue with wear lead to the development of Gas Bearing technology in the late 1950's and early 1960's. For mechanical bearings of the size suitable for load bearing goniometry, runout errors in the order of 2–5 µm can be achieved [11]. For a multi-axis goniometer, the cumulative error from the individual bearing inaccuracies can result in an overall sphere-of-confusion in the order of 10 µm, which is larger than desired for with the new instrument. As these errors can be non-repeatable, there is limited scope for dynamically correcting

them via the motion control system. As air-bearings have smaller, systematic, runout errors, which will not change over repeated use due to wear, they are the most promising means for achieving the smallest possible sphere-of-confusion. Consequently, they are used for the major rotation axes of the new goniometer.

2.2. Properties of the Air-Bearings Used in the Goniometer

Before discussing the specific details of the design and performance of the air-bearings used in this instrument, it is worthwhile examining some of the attributes of the technology that led to their adoption.

2.2.1. Inherent Accuracy

When a shaft is rotated on a "thin" film of air, typically 10 μm thick, the spin axis of the shaft will rotate significantly more accurately than any manufacturing deviations would appear to indicate. For example, the precision of a shaft formed on a cylindrical grinding machine, will generally be of an elliptical figure such that the major axis will be 0.6 μm larger than the minor axis. Yet, the rotational accuracy of the spin axis of the shaft will not deviate, when measured against the best metrological references, by more than a few nanometres. This accuracy is, more often than not, a reflection of the random noise level in the instrumentation.

The reason for this performance is that a pressurised air film will average out the inaccuracies in the shaft thus causing the shaft to rotate about its centre of volume. In fact, the air film is akin to an infinite number of opposed springs acting on the external diameter of the shaft. This property also applies to thrust bearings, or any regular, symmetrically shaped object.

2.2.2. Absence of the "Stick Slip" Effect

When a shaft is supported on ball bearings there will be small differences in drag torque due to relatively high localised stresses between the balls and bearing surfaces and also cage contact. If the shaft is stationary and then caused to move, the breakaway torque can be transiently higher and unpredictable. Over time this can cause micro pits in the bearing surfaces which precludes repeatable movement in sub arc second increments. As the air-bearing has no physical contact between bearing surfaces this problem does not occur and allows repeatable angular movements at the level of sub arc seconds during the life time of the instrument. This absence of physical contact also ensures a long working life for the instrument.

A more detailed discussion on the subject of air-bearings can be found in references [12,13].

2.2.3. Air-Bearings

Details of the Air-Bearings Used in the Goniometer

Two air-bearings are used in the goniometer. The largest air-bearing, the ω-axis, runs with the spin axis held horizontally. The second air-bearing, the φ-axis, is fixed to a bracket fastened to the ω-axis shaft. The φ-axis is set to an angle of 54.74° with reference to the spin axis of the ω bearing and can, therefore, orbit around the ω-axis, whilst spinning about its own axis.

Air-Bearing Design Philosophy

The design of an air-bearing requires that it adequately supports the load to be carried whilst using compressed air of between 5.4 and 6.8 bar (gauge): i.e., air pressures in common industrial use. This level of air pressure, in turn, determines the dimensions of the journal and thrust bearings because the load carrying capacity arises from a mean effective air pressure acting across the projected area of the surfaces.

However, the performance of the goniometer also requires that the air film separating the bearing surfaces produces film stiffness such that any mass/spring resonances are at a frequency significantly

higher than would be encountered in its operation and requires an air film thickness in the range of 10 μm to 12.5 μm. This film thickness applies to both journal bearings and semi-axial air films in the case of thrust bearings, see Figure 2. Air film stiffness is inversely proportional to film thickness. The thickness of the air films need to be controlled to ±10% of the nominal thickness, by careful manufacturing.
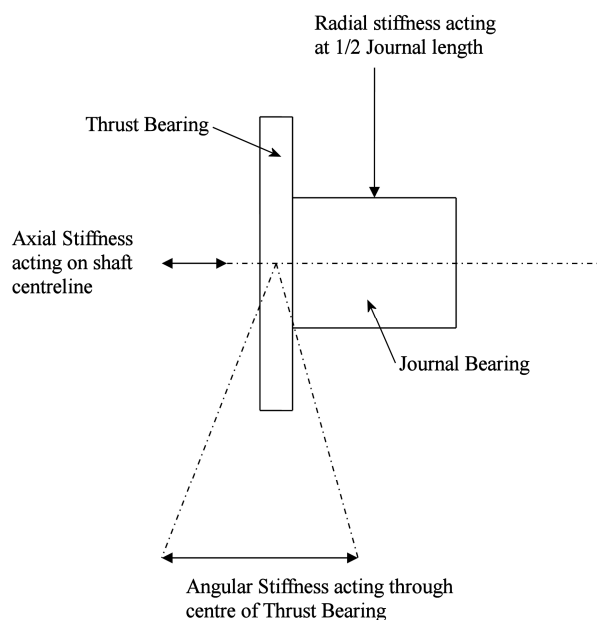

Figure 2. A schematic view of the rotary section (the only moving part) of an air-bearing and the planes of action of stiffness. This section is contained within the casing of the air-bearing assembly and floats on a film of high-pressure air. The journal bearing is composed of a cylinder that bears the radial weight of the load. The thrust bearing is in the form of a disc and it is attached to the journal bearing to prevent a displacement along the axis of rotation (the shaft centerline). For the φ-axis, the thrust bearing has a particularly important role as the load is subject to variations during a rotation of the ω-axis.

2.2.4. Properties of the ω and φ Air-Bearings

The overall dimensions and mechanical properties of both the ω and φ bearings, at a supply pressure of 5.4 bar, are listed in Table 1 below and illustrated in Figure 2.

Table 1. Properties of the ω and φ bearings used in the goniometer.

Bearing Attribute	Properties of ω Bearing	Properties of φ Bearing
Journal Bearing	Diameter = 127.0 mm, Length = 127.0 mm	Diameter = 76.2 mm, Length = 76.2 mm
	Radial Stiffness = 3.5×10^8 Nm^{-1}	Radial Stiffness = 1.27×10^8 Nm^{-1}
	Air flow = 7.0 L/min (free air)	Air flow = 7.0 L/min (free air)
Thrust bearing (two opposed faces)	External Radius = 139.7 mm, Internal Radius = 65.0 mm	External Radius = 86.2 mm, Internal Radius = 38.1 mm
	Axial Stiffness = 1.76×10^8 Nm^{-1}	Axial Stiffness = 6.2×10^8 Nm^{-1}
	Angular Stiffness = 9×10^6 Nmrad^{-1}	Angular Stiffness = 1.13×10^6 Nmrad^{-1}
	Air Flow = 42.5 L/min (free air)	Air Flow = 42 L/min (free air)
Overall Runout Error	0.5 μm	0.25 μm

2.2.5. Air Supply to the φ-Axis Bearing

The φ-axis bearing is retained by a bracket fixed to the ω-axis shaft and rotates about that axis. It is necessary to supply air to the φ-axis without causing mechanical restraints. This has been achieved by constructing an air "slip-ring" on the ω-shaft. The principal of the "slip-ring" can be seen in Figure 3. Essentially, compressed air is passed through the wall of the ω air-bearing body and leaks to atmosphere through the air film, whilst simultaneously supplying compressed air to the φ-axis bearing. There is an overall sacrificial loss of air through the air slip-ring which amounts to 47 L of free air per minute.
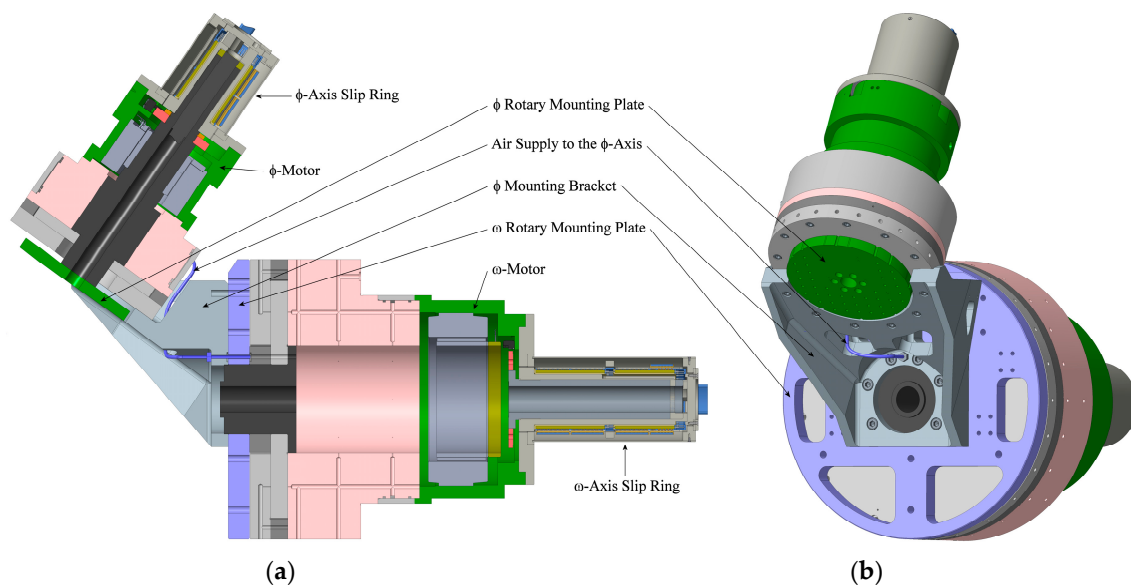

(**a**)   (**b**)

Figure 3. The dual air-bearing goniometer. (**a**) A cut-away view of the air-bearing assemblies showing the paths of the air-flows and cross-sections of both the DC-brushless motors and the electrical slip-rings. (**b**) A perspective view of the dual air-bearing goniometer detailing the φ-axis bracket.

The air slip-ring concept has been utilised previously by Fluid Film Devices in other high-precision instrumentation such as the devices used in the manufacture of Blue Ray master discs.

2.2.6. The φ-Axis Bracket

A key element of the goniometer design is the bracket holding the φ-axis to the ω-axis. The weight of the φ-axis is considerable, amounting to approximately 35 kg, and the bracket will be subject to asymmetric loads as ω is rotated. The stiffness of the bracket is, therefore, a particular concern for the overall sphere-of-confusion of the goniometer.

The bracket was designed with the aid of finite element analysis (FEA). A number of iterations of the design were required to maximise the stiffness while not adding excessive weight. The design of the bracket also required that it did not restrict the range of rotation of the ω-axis at the minimum detector distance.

The FEA calculations were performed within the ANSYS Workbench Platform [14] and carried out with the ω-axis set at 0°, 90° and 180° with respect to the vertical. The flex of the whole goniometer assembly was assessed, including the rotary mounting plate on the ω-stage which part of the bracket would be attached to, see Figure 4. The final design, shown in Figure 3b, has a fairly complex shape composed of two sections. The main section of the bracket is mounted to the journal bearing of the ω-axis, through the ω rotary mounting plate, and holds the φ-axis via the body of the air-bearing at the surface where the φ rotary mounting plate is connected. The second, and smaller, section of the bracket connects to the opposite end of the φ air-bearing body and is attached to both the main section

of the bracket and the rotary mounting plate on the ω-stage. This reduces the "nodding" action of the φ stage as ω is rotated from 0° to 180°. The FEA calculations reveal that the vertical sag, below the rotation vector of ω, is approximately 3 μm for both the 0° and 180° ω settings while the sag at 90° in ω is approximately 2 μm. Overall, the sample position was predicted to deviate by no more than 1 μm vertically, or along the beam direction, at an average position ~2.5 μm below the ω rotation axis. The movement along the direction of the ω-axis was expected to be in the order of 6 μm with the extremes of this displacement, due to the φ-axis nodding action, of approximately +3 μm and −3 μm (in the sense of x in the Diamond coordinate system) at ω = 0° and 180° respectively.

(a)　　　　　　　　　　　(b)　　　　　　　　　　　(c)
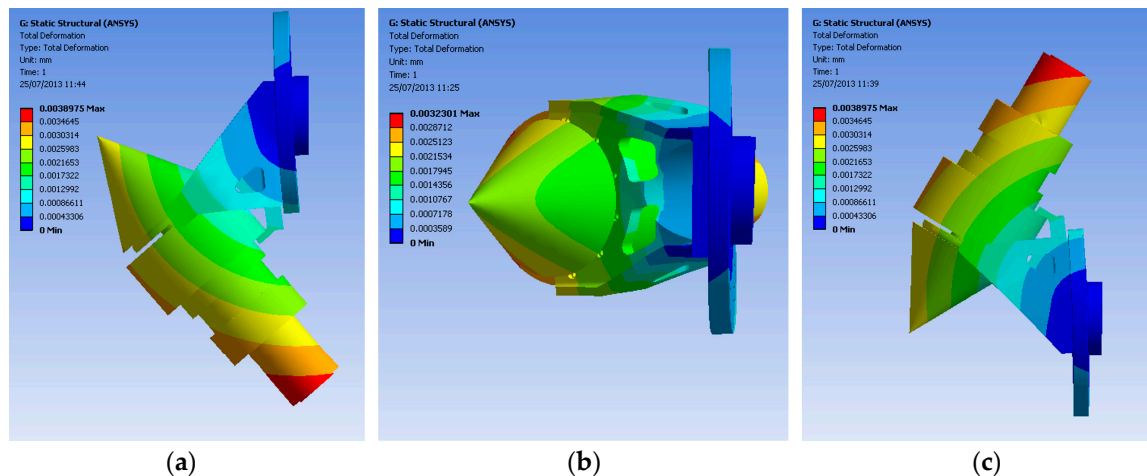
Figure 4. Deformation map for the goniometer from the FEA calculations: (**a**) for ω = 0°; (**b**) for ω = 90°; and (**c**) for ω = 180°. The scale is shown as the degree of deflection in mm.

Given the very small runout errors of both the φ- and ω-axes, the main contribution to the overall sphere-of-confusion was expected to originate from the flexing in the φ-axis bracket and as this flex is purely elastic, and therefore reproducible, it was anticipated that the sphere-of-confusion could be corrected dynamically using the sample stages. The bracket was manufactured by Acrona Engineering Ltd. [15].

2.2.7. The φ-Axis, ω-Axis and Sample Stage Motions Hardware

The φ- and ω-axes are equipped with KBMS-25 H-A00 and KBMS-57 H-02-A00 Brushless Motors respectively (supplied by Heason Technology Ltd. [16]) which were interfaced with bespoke electrical slip-rings for all connections, supplied by Pandect Precision Components Ltd. [17]. Both stages incorporate a pair of Renishaw [18] incremental encoders (type No. Tonic T260130M), which are mounted at orthogonal positions on each circle, and Renishaw scale rings (REXM20USA075) with diameters of 115 mm and 75 mm (which give 18,000 and 11,840 cycles per revolution) for ω and φ respectively. The encoders are interpolated, using Renishaw TONIC Ti1000, to give 0.349 μrad (50,000 counts/deg) and 0.531 μrad (32,889 counts/deg) respectively. The additional encoder on each axis currently acts as a backup, in case of failure of the primary encoder, although there is the potential to use both in parallel to eliminate errors and provide additional precision. Hall sensors incorporated within the motors provide supplementary controls information for angular positioning. The φ and ω stages have channels through their rotation axes to provide a route for the electrical cables. The cables associated with the sample stage are routed through the φ-axis and its slip-ring, while all the cables associated with both the sample stage and φ-axis are routed through the channel in the ω-axis emerging through its slip-ring.

The sample stage is composed of three PM-Bearings [19] linear piezo stages (RTP-1510-0.1 micron), each incorporating Numerik Jena encoders (LIK41, 0.1 micron resolution). The stages are mounted

such that they are sufficiently offset from the centre of the φ rotary mounting plate to provide clearance for the electrical cables. A set of brackets are attached to the φ rotary mounting plate to hold the three encoder connectors and the connectors supplying power to the piezo linear motors. The encoder brackets are also used to attach a conical cover over the sample stage assembly which assists in the management of the cables. The conical cover was 3D printed to a thickness of 1 mm in aluminium (grade CL31) by CA Models, Stirling [20]. The sample z-stage (which is mounted orthogonally, via a bracket, with respect to x,y-stages) contains a magnetic kinematic base to which the sample stick is secured. The sample stick is designed to detach if there is an extreme load applied to it by the robotic sample changer to protect the piezo motors. The sample itself is attached to the stick via a magnetic mount for MiTeGen micromounts, or other suitable loops, on SPINE pins with a length of 17.6 mm.

2.3. The 2θ Circle, Detector Arm and Detector Translation Stage

Both the rotation and translation stages for the detector 2θ arm have fairly conventional designs. The 2θ circle is composed of a Huber [11] model 480-X2W1 one-circle goniometer supplied with a model M.OR83.200 stepper motor. The circle is normally supplied with a 1:20 reduction gearbox (model GEAR 2083.20) but this limits the slew rate to a maximum of 0.5°/s. Although the detector 2θ angle is fixed during data collection, this slew rate was considered too slow to be practicable and so the gearbox was replaced with an alternative model offering a 1:5 gear ratio (model GEAR 2083.05). A Vexta clean damper was attached to the drive shaft of the motor. With this modification slew speeds of 1°/s could be achieved for the completed system over the full angular range of the arm and for all possible balance conditions governed by the position of the detector along the arm. The circle was modified slightly to integrate the standard Huber model 480 top plate. The 2θ encoder incorporated a Renishaw Tonic rotary read head (E.RE.T2040-30A) and a Tonic scale tape, with a pitch of 20 μm (E.RE.RGSZ20-S.1200). The limit switches are set to restrict the rotation of the arm to 2θ angles ranging from −30° to +120°.

The 2θ arm was machined from a single piece of aluminium and incorporates a linear translation stage for the detector assembly. The detector support was machined from a block of aluminium and mounted to a pair of THK [21] linear motion guides (type No. SSR20XW) composed of 730 mm long rails with a pair of caged-ball carriages on each rail. The detector support is driven by a ball-screw assembly, (also supplied by THK (type No. EPB2510-4RRG0+638LCP5R-J1)) via a Mclennan 23HSX-series high-performance stepper motor with a brake (type No. 23HSX206CEB24-4295) and an IP57 planetary gearhead with a 10:1 gear ratio (IP57-M01). The motor and gearbox are connected to the detector support via a ball-screw, which is also supplied by THK (type No. EPB2510-4RRG0+638LCP5R-J1). The screw is fixed by a bearing at a single point on the arm (close to the motor assembly) so that the screw can "float" on the flexible coupling to the gearbox and prevent binding. The stage incorporates a Renishaw incremental encoder (type No. Tonic T260130M), and a 20 μm pitch Tonic scale tape. The extremes of travel are protected by limit switches. The 42 kg Pilatus 2M detector can be driven at 5 mm/s over the full 2θ range (from −30° to +120°) although higher speeds, up to 10 mm/s can be achieved between −30° to +30° when there is less gravitational load on the drive system.

The detector is mounted so that at 2θ = 0° the beam does not align with the geometrical centre of the array of sensor tiles. This ensures that all reflections can be collected from a single φ or ω rotation with only a pair of reflections, from the set of 4 possible equivalents, falling within a gap between panels.

2.4. The On-Axis Viewing Camera

One of the great benefits of a third generation light source is the relatively large distances between the source, the optics and the sample. This allows the incorporation of a range of diagnostic elements into the long beam path. In protein crystallography, for example, the space immediately upstream of the sample position, and beam collimating elements, has been occupied by an on-axis viewer (OAV),

which is essentially a microscope containing a periscopic arrangement of mirrors. In this geometry, the X-ray beam is directed to the sample through holes drilled in the objective lens and first mirror on the optic axis. With this arrangement, the users can view the sample along the same path as the X-ray beam. The OAV, therefore, enables the rapid alignment of the beam to the goniometer centre through the use of a fluorescent screen that can be placed in the beam, and subsequently retracted, via a set of motorised stages. The final X-ray collimation is provided by a beam defining pinhole, and its associated scatter guard, placed between the objective lens of the OAV and the sample position. To allow sample viewing and alignment between data collections the collimation is withdrawn on a series of motorised stages, see Figure 5.
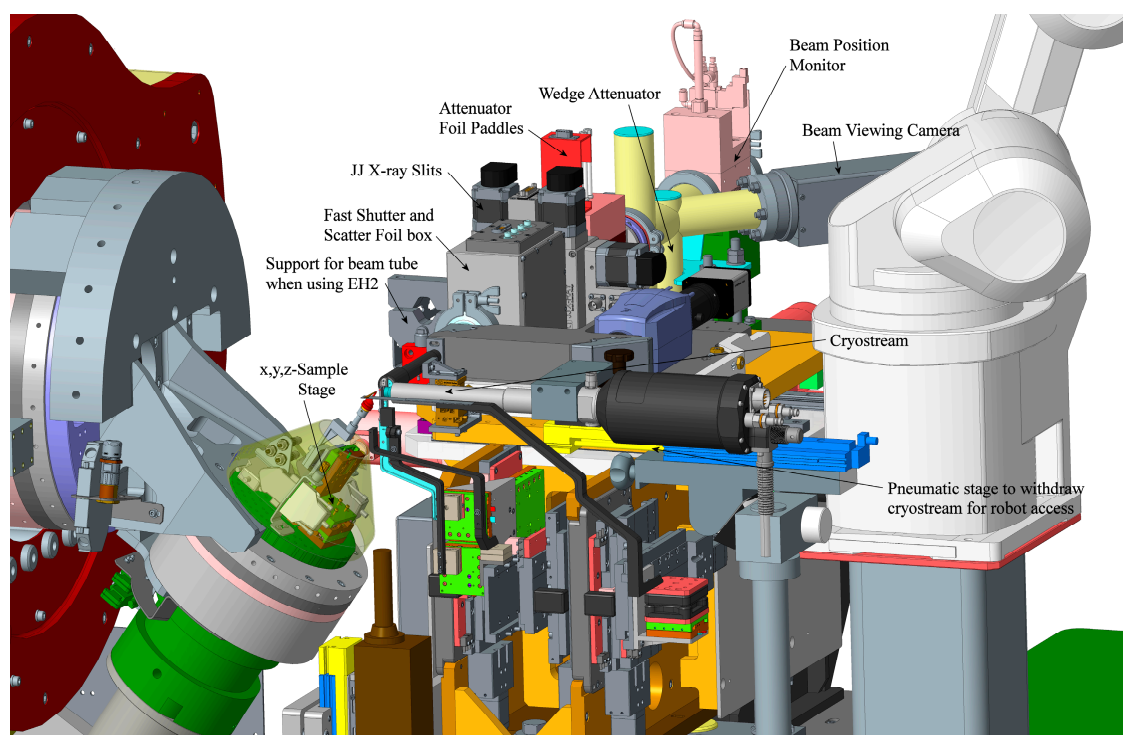

Figure 5. Detailed view of the sample stages, on-axis viewer and beam conditioning assembly. The conical cover has been shown as transparent to allow the x,y,z sample stages to be viewed. The detector has been omitted for clarity.

The space envelope available for the OAV system of the new diffractometer meant a degree of reworking of the Diamond MX design was needed, see Figure 6. Space was required by the φ-axis in order to allow an unhindered rotation of the ω-axis to which it is mounted. As the objective lens (supplied by Qioptiq [22]) has a 35 mm working distance (focal length), it is placed within the potential collision range of the sample mount and, therefore, its diameter had to be reduced from 25 mm to 16 mm (by Agate Products Ltd. [23], who also drilled the 1 mm holes through the objective lens and the first mirror) to give enough clearance. Additionally, the distance between the lens and first mirror had to be increased significantly over the original MX design. The lens is, therefore, held in a tube mounted to the OAV base plate via a Newport [24] compact dovetail linear x,y,z manual stage (model: M-DS25-XYZ), which provides lateral adjustment relative to the optic axis and a means of fine focus. The periscope assembly is machined from a single aluminium block and this provides support for: both of the mirrors, with the second mirror mounted on a set of tilt adjustment screws; the Qioptiq [23] Fetura Advanced Zoom Lens System (model 42-35-37-000) and TV tube; along with the CCD colour viewing camera (Allied Vision [25] Prosilica GigE). When the optics are correctly set up, the zoom system allows the sample to remain in focus, without further adjustment, over its entire magnification

range. Due to the optical vignetting introduced by reducing the diameter of the objective lens, the zoom system is used through just 30% to 90% of its range.
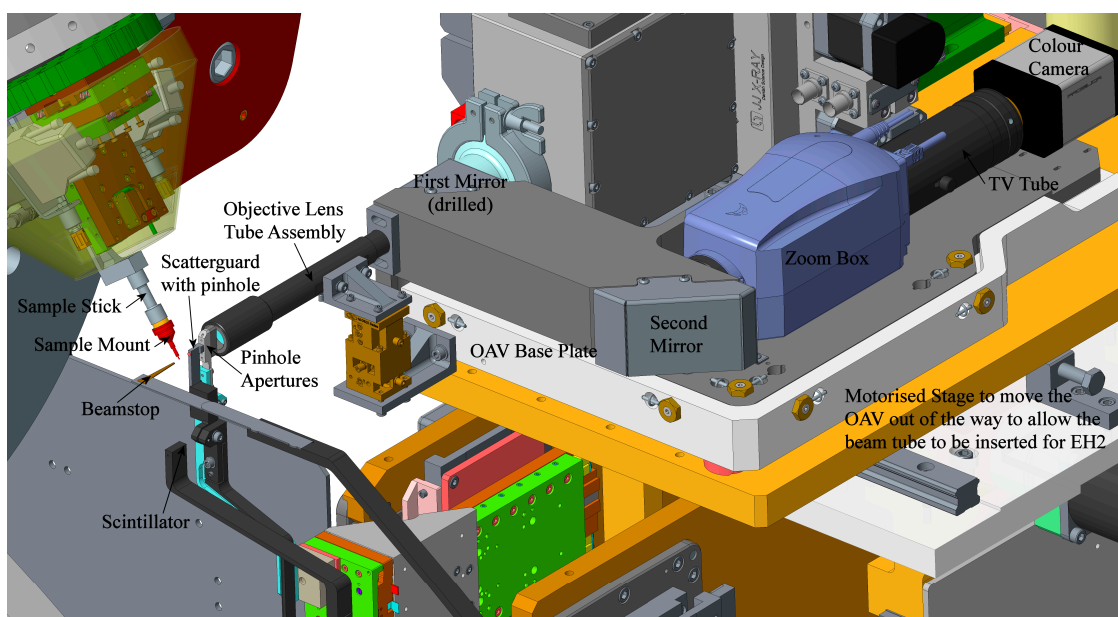

Figure 6. Detailed view of the on-axis viewer assembly and beam conditioning "sticks" located in the vicinity of the sample. The ω-axis is shown at 180°.

The periscope assembly is braced to the OAV base plate via a set of tensioned springs with the block of the assembly floating on micrometre threaded screws. This arrangement provides a means of fine adjustment in height, roll and pitch, while a second set of screws and springs set horizontally offer limited yaw and focus correction. The base plate of the OAV is held on to the beam conditioning assembly kinematically via a set of tooling balls and pads.

2.5. The Beam Conditioning Assembly Containing: The Beam Collimation and Beamstop Stages; the Fast Shutter and Beam Diagnostic Assembly; the Beam Defining Slits; and the Attenuators

The OAV is mounted to the beam conditioning assembly via a motorised stage that also supports the fast shutter, beam diagnostic assembly, beam defining slits and attenuators. If beam is required in the second experiments hutch (EH2) of the beamline, the stage can be translated horizontally for the positioning of an evacuated tube to provide a suitable beam path. This arrangement does not disturb the alignment of the diffractometer with respect to the beam and allows user operation to be switched between hutches in less than half an hour. The beam conditioning assembly is composed of two main sections: the lower section is secured to the jacking table while the upper section, which contains the motion stages, is supported on three screw jacks which give height, pitch and roll adjustment. A set of bolts provide a means to adjust the upper assembly along the beam direction, to set the OAV at approximately the correct focus, and across the beam horizontally in both position and angle (yaw).

The fast shutter has a relatively simple design being constructed from a slotted tungsten cylinder connected to a rotary solenoid. The shutter is opened when the solenoid rotates the slot parallel to the beam. The shutter box also contains a pair of kapton scatter foils placed on either side of the shutter so that the beam flux both before, and after, the shutter can be recorded on photodiodes. To improve the measured signal a pair of diodes is used on each scatter foil.

Upstream of the shutter box, a set of slits supplied by JJ X-ray [26] (IB-C30-HV with rotary encoders on the motors for each of the 4 blades) is used to initially define the beam size prior to final collimation in the apertures adjacent to the sample position. Drain currents can also be measured from each of the blades to provide information on the beam position.

The final element on the OAV stage (which is also translated out of the beam for EH2 operations) is a set of four attenuator paddles that contain aluminium foils of different thicknesses (2 mm, 1 mm, 0.5 mm and 0.25 mm). These can be used individually or in combination to alter the beam transmission in the range from 100% to 1% at the most frequently used wavelength (0.6889 Å the Zr K edge) on the beamline. A second attenuator placed further upstream of the diffractometer in EH1 is useful at short wavelengths. This attenuator is composed of a wedge-shaped block of aluminium which can be translated progressively into the beam to provide the required beam transmission. As the wedge attenuator is left in the beam path it is also used for operation in EH2.

The motorised stages for the X-ray collimation, beamstop and scintillator are mounted at one end of the fixed assembly beneath the OAV. The X-ray beam diameter can be defined by the selection of one pinhole from a set of three, each with a different diameter (currently one location is vacant while the other two positions contain 100 μm and 50 μm pinholes), mounted within the pinhole holder, or "stick". This assembly is mounted via a magnetic kinematic base (supplied by Thorlabs [27]) to a motorised x,y,z-stage. The pinholes are clamped into apertures within a tungsten block oriented vertically on the stick and a pinhole can be selected by driving to the appropriate position using the y-stage. Fine alignment of the pinholes relative to the beam is performed by scanning the x- and y-stages in turn, while the positioning of the pinhole stick along the beam direction is adjusted by the z-stage. The stick is usually positioned to provide approximately 1 mm clearance between the pinhole block and the objective lens of the OAV. Both the y- and z-stages are conventional stepper motor driven worm–gear assemblies (Parker [28] MX80S stages, ball-screw with 0.1 μm Renishaw encoders) to provide a sufficiently long-stroke to fully retract the pinhole stick for sample mounting (either by hand or through the use of the robot) and to allow sample viewing and alignment between data collections. The x-stage is of the stick-slip piezo motor variety (RTP-1510 and RTP-2035 stages from PM Bearings with RGH34 encoders and 0.1 μm RGS linear scales). As the pinholes produce scatter that would otherwise contaminate the diffraction images collected by the detector, a scatter guard consisting of a secondary pinhole with a diameter of 200 μm (larger than those used to collimate the beam) attached to a tungsten block with a 1 mm hole (stepped down to 0.6 mm at the point where the pinhole is attached) drilled through it, is placed immediately downstream of the pinhole assembly to allow the beam to pass cleanly through while stopping the scatter. The scatter guard stick is kinematically mounted to a set of piezo x,y-stages which piggy-back the pinhole assembly. This arrangement allows the scatter guard to be aligned independently to the pinhole and allows both the pinhole and scatter guard to be withdrawn from the beam simultaneously with one stage (the long-stroke y-stage for pinhole assembly) without affecting any of the other axes. The scintillator stick is kinematically mounted to a pair of long-stroke y,z-stages to allow complete retraction of the assembly when it is not in use. As the scintillator stick can be aligned with sufficient accuracy, using the lateral translation bolts of the upper section of the beam conditioning assembly, a motorised x-stage is not required. The scintillator material is a 2 mm diameter 0.1 mm thick YAG:Ce crystal supplied by Crytur [29]. Finally, the stick for the beamstop is mounted to a set of long-stroke stages to provide movement in the y and z directions, so that it can be fully retracted for sample mounting, and fine adjustment in the x direction is provided by a piezo stage. As the cryostream open-flow cryostat is mounted horizontally, and the nozzle needs to be placed approximately 5 mm from the sample, the design of the beamstop stick had to take the positioning of the cryostream head into consideration so that the beamstop could be placed sufficiently close to the sample position.

2.6. Backlight and Backstop Diode Assembly

As the OAV camera requires a powerful backlight to allow accurate sample alignment at all zoom settings, a source of illumination needs to be placed behind the sample during crystal centring which must then be withdrawn for data collection. This is carried out on the MX beamlines via a flat-panel LED light, supplied by Keyence Ltd. [30] placed on a pneumatically operated piston. These pneumatic devices have sufficient positioning accuracy, and reproducibility, for this function and they

have the advantage of being extremely fast and free from the complications of a motorised stage. The same approach was adopted for the OAV camera in this diffractometer design. As the backlight needed to retracted over a longer distance than could be accommodated by a single piston (given the distance between the sample position and the top of the jacking table and the clearance required for the detector at its minimum distance to the sample at a setting of $2\theta = -30°$), two pistons were coupled in series via a bracket. The two cylinders are parallel when fully retracted and nearly end-on-end when totally extended. This approach effectively doubles the range of a single-cylinder while maintaining a compact design when retracted.

The MX beamlines also perform a check to ensure that the beamstop has been aligned correctly before each data collection. This is carried out by placing a retractable diode, which is suitably attenuating to block the beam, downstream of the beamstop while the fast timing shutter is opened. If a signal is recorded above background, this indicates that the beamstop is out of position and the data collection is stopped in an error state to protect the detector. A similar approach has been adopted in this diffractometer design where, instead of using a retractable panel mounted onto the detector itself, a second pneumatic piston (supplied by IMI Precision engineering [31]) is placed downstream of the backlight. The piston is piggy-backed to the coupling bracket of the backlight meaning the lower pneumatic piston is tasked with supporting both the backlight and diode.

2.7. The Cryostream Mount Assembly

A key element of modern crystal structure determination is the use of an open-flow nitrogen cryostat to cool the sample. Its use both increases the resolution of the diffracted intensities (due to the suppression of thermal motion) and provides a means of protection for air sensitive samples or samples sensitive to solvent loss. Cooling the sample also mitigates the effects of beam damage at high-brightness sources which is especially the case at synchrotrons. The effective working distance between the sample and the end of the nozzle for a Cryostream [32] is approximately 5 mm but this leaves insufficient space for the action of the end effector (gripper) of the robotic sample changer. During a sample change the distance needs to be increased momentarily (by approximately 10 mm) to allow the end effector access. This was achieved by incorporating a pneumatic translation stage [31] into an adapted Cryostream stand. The stage is synchronised to the action of the robot so that the Cryostream can be withdrawn for the period that the end effector is at the sample position of the diffractometer. This period is short enough to prevent either icing on the sample, if they have been stored cryogenically, or sample degradation due to momentary warming. (For studies requiring lower temperatures, such as electron-density studies, the Cryostream assembly can be repositioned to allow the use of a Helix open-flow helium cryostat [32]. A separate removable stand, which is bolted to the floor of the hutch, is used to support the Helix.)

2.8. X-ray Fluorescence Detector Mount

One of the principal advantages of synchrotron radiation for the study of small-molecule systems using single-crystal diffraction techniques is the ability to vary, or tune, the photon beam energy to match the absorption edge of an element within the sample for anomalous dispersion studies. To tune to the specific energy required, fluorescence scans are performed by making use of energy-sensitive detectors to measure the photons scattered by the sample as the energy is varied. A Vortex 90EX Silicon Drift Detector [33] is used for these fluorescence experiments and this is mounted to the diffractometer via a bracket on the fixed lower section of the beam conditioning assembly. The detector is secured to a pneumatic translation stage [31] so that the entrance window can be placed close to the sample position when a fluorescence scan is being performed. To prevent a collision with the φ-stage, the pneumatic can only be extended when the ω-axis is rotated to the $-90°$ position (so that the φ-axis is placed adjacent to the OAV). After the fluorescence scan has been completed, the ω-axis can only be moved from this position once the fluorescence detector has been fully retracted.

3. Motion and Controls Systems

The motion controls of the diffractometer are handled by EPICS (Experimental Physics and Industrial Control System) software. This is a suite of open-source software tools, libraries and applications that have been developed to create control systems for scientific instruments such as particle accelerators, telescopes and other large scientific experiments [34]. It is used throughout the Diamond Light Source infrastructure from the synchrotron accelerator controls through to the beamline components and end stations. For the diffractometer controls, the EPICS software layer communicates with an Input/Output controller (IOC) running on a Linux server which in turn drives the motor control hardware. The motor controllers are Delta Tau Geobricks (GeoBrick LV IMS II) which are interfaced with EPICS using a model 2 PMAC asyn driver [35]. The EPICS motor records are mounted above the driver and allow position demands, velocity and acceleration to be set. As well as controlling the basic motion of the various axes on the diffractometer, the EPICS layer also handles collision avoidance between the detector and the goniometer. This is achieved through a look-up table accessed via an EPICS genSub record which checks, at a rate of 10 Hz, the positions of ω, 2θ and detector distance, setting limits on these axes accordingly. If the axes are moved individually, or simultaneously, the dynamic limits will prevent a collision by stopping the affected axis at the limit. As an additional precaution, a rubber compression switch, in the form of a "picture frame", has been added to the detector as a hard limit [36]. EPICS also ensures that the pneumatic axes, which hold the backlight and backstop diode (along with the pneumatic stage for the fluorescence detector) cannot be deployed unless the ω-axis, 2θ-axis and detector distance are sufficiently clear.

The synchronisation of signals from the Geobricks, Pilatus 2M detector and ω and φ axes encoders for data collection scans is handled via Zebra cards, which have been developed by the controls group at Diamond to simplify the interlacing and generation of trigger and gate signals where a range of devices need to be choreographed in real time [37].

The diffractometer system has a total of 27 motion axes (covering the brushless motors of ω and φ, stepper motors, piezo linear stages, pneumatic axes and the control of commercial hardware, such as the Fetura zoom system), all controlled from 3 Geobricks. These, along with an additional spare Geobrick, their power supplies and the pair of Zebra cards, are housed in two three-quarter height racks, situated on the roof of EH1. The control cables are routed to the diffractometer through custom-made electrical chicanes and the entire system, which is otherwise stand-alone, communicates with the beamline infrastructure via the local computing network.

Dynamic Correction of the Sphere-of-Confusion

The use of Zebra cards in the motion control system allows mixing of encoder signals from the sample x,y, and z stages, with those from the ω and φ axes of the goniometer. Therefore, complex synchronisation of these axes can be carried out for a dynamic correction of the sphere-of-confusion with the required precision. As both the ω and φ axes have extremely small runout errors, the most significant contribution to the sphere-of-confusion is from the flex in the φ-axis bracket and, given that this flex is completely elastic and entirely reproducible, the deflection of the sample position can be accurately mapped as a function of ω and incorporated in the controllers as a set of look-up tables.

The results of the sphere-of-confusion measurements, and subsequent correction, are illustrated in Figure 7 where a ruby sphere (of 20 μm diameter) is shown mounted on a MiTeGen loop and positioned at the instrument centre with ω = 0° (where it has been centred on the φ-axis rotation at the correct height to bring the sample onto the ω rotation axis). The runout error of the φ-axis was found to be less than 1 μm in the plane perpendicular to the OAV camera and in the direction of X-ray beam, Figure 7a. The runout in φ was found to be less than 1 μm for all possible orientations of ω and, therefore, there are no φ-dependent aberrations in the sample position that need to be considered for the sphere-of-confusion correction.
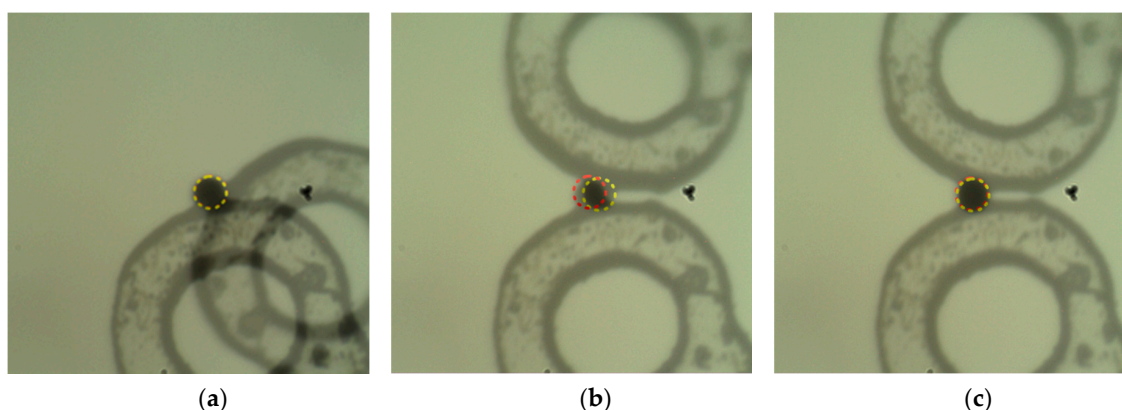
(**a**)   (**b**)   (**c**)

Figure 7. The on-axis viewer images of a 20 μm diameter ruby sphere mounted on a MiTeGen loop and centred on the φ-axis rotation at the height to bring the sample onto the ω rotation axis. (**a**) An overlay of images with φ at 0° and 180°, and with ω = 0°. The ruby sphere is indicated by the red dashed circle at φ = 0° and the (overlapping) yellow dashed circle at φ = 180°. (**b**) The overlay of images with ω = 0° and φ = 0° (ruby sphere indicated by red dashed circle) and ω = 180° and φ = 0° (ruby sphere indicated by yellow dashed circle) with no correction applied. The displacement of the position of the ruby sphere is 7.5 μm along the direction of the ω-axis (horizontal). (**c**) The overlay of images with ω = 0° (φ = 0°) and ω = 180° (φ = 0°) with the sphere-of-confusion correction applied. The translation of the centre of the ruby sphere (indicated by the red and yellow dashed circles for ω = 0° and ω = 180° respectively) is less than 2 μm.

A rotation of 180° in ω is illustrated in Figure 7b, where a movement of 7.5 μm in the sample position along the direction of the ω-axis is observed (indicated by the ruby sphere). This movement is in excellent agreement with the predictions of the FEA calculations and the expected nodding motion of the φ-axis, see Section 2.2.6.

In order to provide a look-up table for the sphere-of-confusion correction, the pixel OAV offsets were mapped as a function of ω and converted into the x,y,z sample stage translations: i.e., the movements that would be required in the stages to bring the sample back to its initial starting position at ω = 0°. These initial corrections were only valid for the starting φ position at which the offsets were determined (which was at φ = 0°). For a correction at arbitrary angles of φ, an additional trigonometric correction is applied to the sample stage x,y,z positions to ensure that the sample is returned to the corrected instrument centre, chosen to be at the ω = 0° position (the position indicated by the dashed circle in Figure 7a at one extreme of the nodding motion).

The overall effect of the dynamic sphere-of-confusion correction is shown in Figure 7c where an OAV image of the sample at ω = 0°, is overlayed with a corresponding image of the sample following the correction at ω = 180°. The movement in the sample position between these two extremes in the nodding motion is within 2 μm and indicates a substantial improvement in the overall sphere-of-confusion for a complete ω rotation.

As the correction for the rotation of the ω-axis has displaced the sample from the centred position on the φ-axis, any rotation of φ at a non-zero ω angle will result in the sample orbiting the φ-axis at a distance of the calculated offset for the x and y sample stages. Therefore, in order to perform a φ data collection scan at an arbitrary angle of ω an additional dynamic correction for the φ-axis needs to be applied using the same procedures as those adopted for the ω-axis.

Although these corrections have not yet been fully commissioned, it is expected that once they have been applied, data collections can be undertaken with beam sizes substantially less then 10 μm in diameter, thereby greatly improving the signal-to-background for micron sized samples.

It should be noted that the measurements were carried out with the Crysostream switched off so that there was no cold nitrogen gas flow over the test sample. It has been found that the force of the gas flow can flex the MiTeGen loop thereby displacing the perceived centre of rotation of the

instrument. As the flow of the crysotream is directed along the rotation axis of the ω-circle, the overall effect is to move the centre of rotation of the goniometer in the order of 10 μm along ω towards the diffractometer (i.e., in the direction of the Cryostream flow). As the force of the gas flow on the sample is unaffected by the angle of ω, this configuration is found to be stable and the sphere-of-confusion (both corrected and uncorrected) is as described above. However, as the top of a MiTeGen loop is relatively flat, the deflecting force varies as the area presented to the Cryostream flow changes when φ is rotated. The overall effect can be to increase the φ runout error from less than 1 μm to approximately 3 μm. Therefore, to obtain the best performance from the instrument a small dual thickness loop is required.

4. Robotic Sample Changer

A robotic sample changer can dramatically improve the efficiency of beamtime as a sample exchange takes less than a minute. This is significantly less than the time required to manually change a sample where the user has to reset the hutch interlock, exchange the sample by hand, and then search and interlock the hutch again. The use of a robot also allows the remote operation of the beamline. For MX, this has become the principal mode of operation and users seldom attend the experiment, but simply send their samples to the synchrotron. The samples are placed in the robot Dewar and the users assume control of the beamline from their home institution. At Diamond Light Source sample changes are facilitated by the BART robot system which was initially implemented on the MX beamlines [38,39]. The same system has been adopted for I19 where a Mitsubishi Melfa RV-6S arm, operated via a Mitsubishi Melfa CR2B-574 controller, is used as the core element of the sample changer [40]. Signals between the robot and peripheral equipment are exchanged via a Diamond built PLC crate and the entire system is integrated with EPICS over the local beamline computing network. The Dewar lid is composed of a series of sliding rings with an aperture for the insertion of the robot end-effector, see Figure 8. An image recognition system (composed of an Omron FZ-SC2M camera, an Omron FZ5-L355 control box and Omron CJ2M CPU [41]) is integrated into the PLC and allows the robot to locate the position of the opening automatically prior to an exchange. This system is very convenient for users as the robot will determine the aperture position after the robot Dewar has been loaded with a new batch of samples with no need to accurately pre-align the rings. To minimise icing on the Dewar lid the rings rest on top of a heat mat located at the top of the Dewar. The robot end effector is dried between cryogenic sample exchanges, using a hot air device, to avoid ice formation. The auto-filling Dewar can be used to hold up to 80 samples in unipucks [42] under liquid nitrogen. Cryogenic sample mounting provides the opportunity to preserve mounted samples, including those that are air sensitive or vulnerable to solvent loss, until allocated beamtime. By pre-mounting crystals less time is spent during the beamtime on sample preparation and users can spend more time concentrating on data collection. Further, dry shippers can be used to send pucks of pre-mounted samples to Diamond and users can log in remotely for their beamtime. As the time required for users to travel to Diamond is no longer necessary, it becomes feasible for regular users to have shorter, more frequent, slots of beamtime, allowing them to study crystals in a more timely fashion. In addition to the sample Dewar, a number of room temperature sample trays allow automated sample changing for over 200 samples stored under atmospheric conditions, see Figure 8.

A GDA (General Data Acquisition) script orchestrates the sample exchange process. Before the robot approaches the sample position, the script moves the detector, beamstop, scatterguard and pinhole aperture clear and moves ω, φ and the sample x,y and z stages into place. The cryostream is retracted to allow the robot end effector access to the sample mount but the period is minimised in order to reduce the risk of ice formation on the sample. To prevent accidental collisions, the EPICS controls have a set of safety flags, GPIO (General Purpose Input Output) readback signals, which prevent the robot moving if there is a motion error. A pair of colour sensors (Keyence CZ-H35S [30]) are used as an independent verification to the motor controller signals in the GPIO to ensure that 2θ and ω are both set at $0°$, as commanded by the GDA, before the robot enable is set. To prevent the

robot mounting a sample on top of another already on the diffractometer, the GDA and robot controller keep a record of the most recent action. In case a sample has been mounted by hand, or an error in the sequence has occurred, a pin sensor (Omron EC3-LD11 [41]) monitors the sample position on the diffractometer to check if a loop is in place. The signal from the pin sensor is also flagged in the GPIO and this will prevent a robot action if a mount command is received. The final diffractometer assembly is shown in Figure 9.
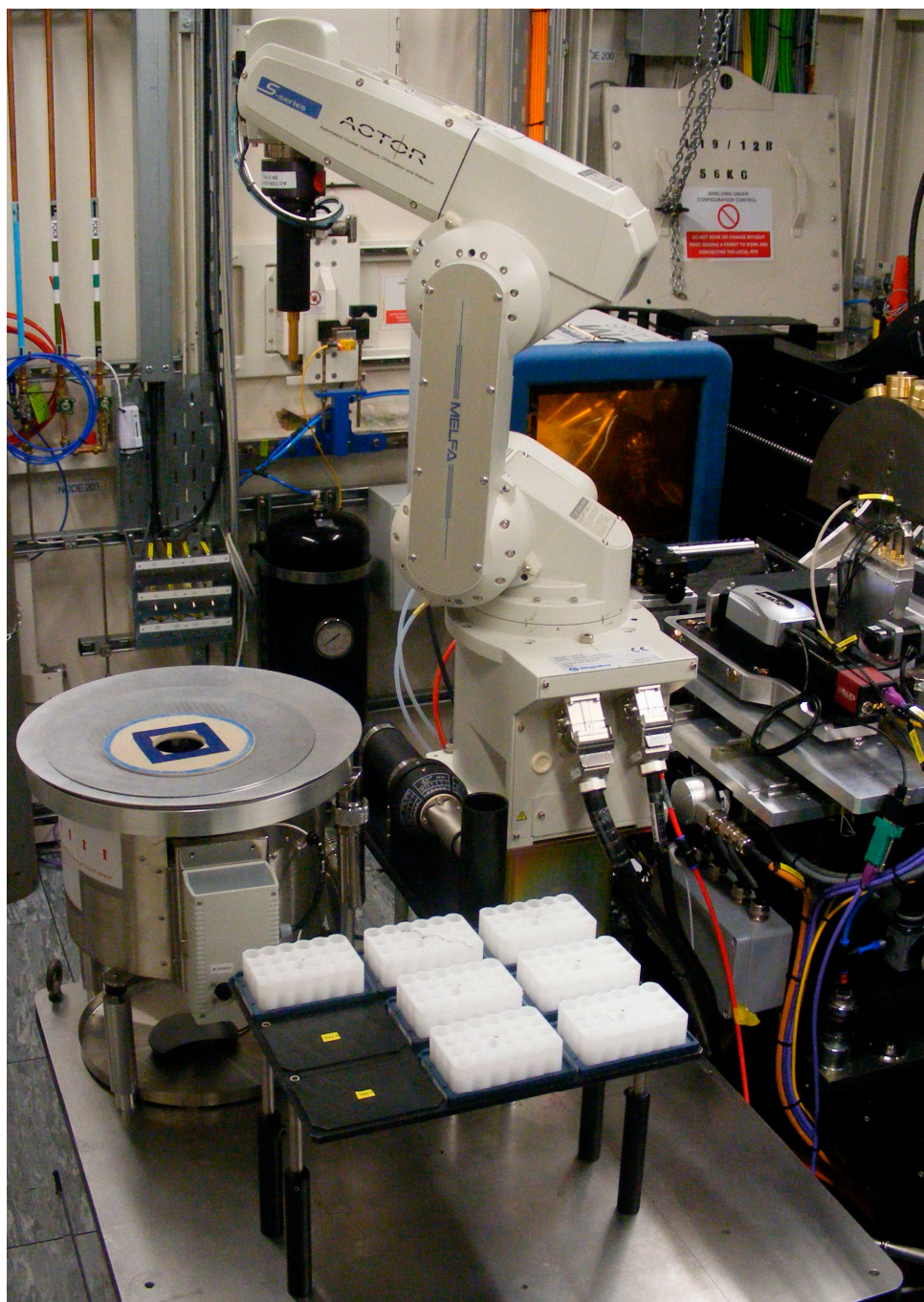
Figure 8. The robotic sample changer. The Dewar for storing unipucks is shown to the left of the robotic arm while the trays for holding sample mounts under ambient conditions are shown in the foreground. The aperture in the sliding lid of the Dewar is indicated by a blue square inside a blue circle for the image-recognition system. The camera for locating the lid aperture is mounted above the robot table and not shown here.
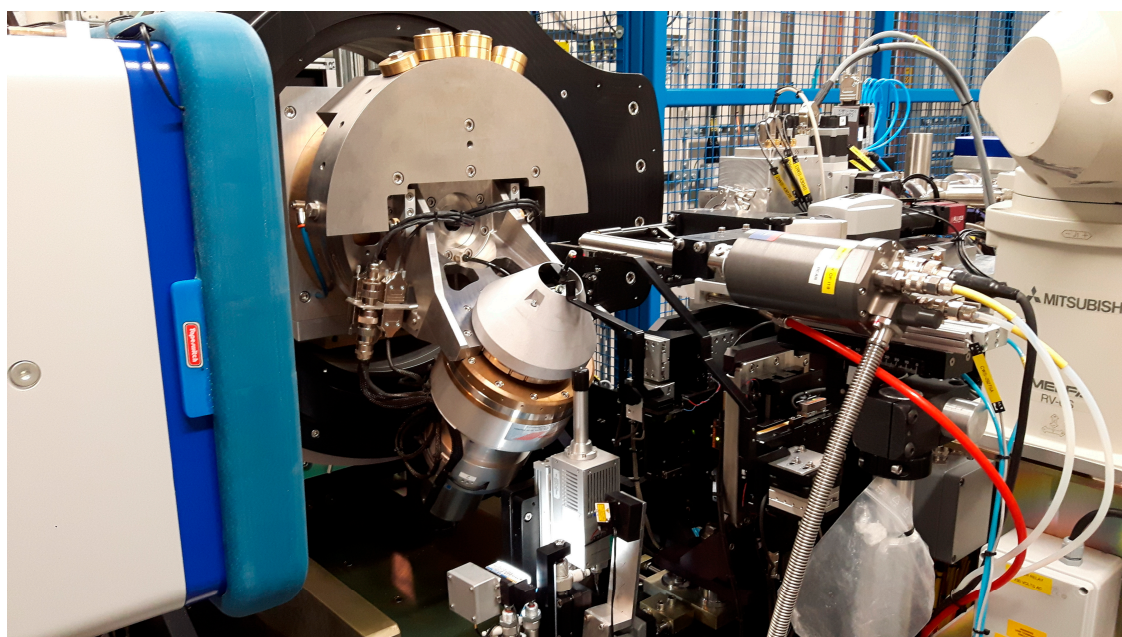
Figure 9. The complete diffractometer system in its fully assembled form. The diffractometer is shown with 2θ = 0°, ω = 0°, φ = 0° and the detector distance set to 300 mm.

5. Data Acquisition and Data Processing

All of the high-level user interactions with the diffractometer are carried out via the Diamond GDA software layer, which coordinates and synchronises the beamline hardware and file systems, including data collection and triggering of post collection data analysis [43,44]. GDA was initially developed at SRS Daresbury, but from 2003 Diamond Light Source became the principal developer having adopted it as the main method of beamline control across the facility. The I19 EH1 GDA borrows many of its features from the MX beamlines at Diamond where several of the core functions have been directly carried over. These features, which have been implemented with only minor changes, include sample cataloguing, the use of the robotic sample changer and the use of the OAV for point-and-click centring of samples on the diffractometer. Cataloguing is carried out by the ISPyB database [45,46] which records information about data collection parameters, sample details, and provides access to results from the automatic processing pipelines.

The data collection features within the GDA have been modified significantly, however, to deal with the requirements for small-molecule crystallography where a number of scans are needed, often at a number of different 2θ settings of the detector, for a complete data set. These adaptations include changes to the data collection scan table to allow a choice of detector 2θ, as well as sample to detector distance, and the option of choosing either ω or φ as the principal scanning axis.

Data processing is carried out automatically via a version of the protein crystallography data pipeline which has been extensively reworked for the requirements of small-molecule crystallography. The screening of crystals, prior to data collection, is a particular concern as the diffracted reflection intensities can show very large variations, which is in contrast to the less extreme intensity differences found in macromolecular crystallography. As an individual pixel on a Pilatus detector can be paralysed when the count rate exceeds a threshold at which more than one photon arrives within the dead-time of the pixel (with the Pilatus 2M detector set to low-gain mode this dead-time is in the order of 0.1 μs [47]), some care is required to ensure that the most intense reflections from the sample crystal are recorded below this limit. If the strong reflections exceed the count-rate threshold their intensities will be systematically underestimated. To avoid this situation, and to assess overall crystal quality, a short screening data collection scan is used after the sample is mounted and centred on the diffractometer.

The data are then automatically assessed via a screening programme (i19.screen) which indexes the reflections recorded on the raw narrow-sliced (usually of 0.1° angular width) images, determines the mosaic spread of the reflections, and histograms the pixels in order of increasing intensity as a fraction of the estimated maximum count rate [48]. From the histogram, it is then possible to determine the degree of attenuation required (if any) for the incident primary beam for the subsequent full data collection. The determination of the mosaic spread of the sample is particularly important for the threshold determination, as the peak count rate for samples with extremely narrow rocking curves can substantially exceed the pre-determined (detector default) threshold averaged over the angular width of an individual image. The subsequent data collection can be composed of a series of ω and/or φ scans at varying 2θ angles and detector distances. The multi-scan data are processed automatically via DIALS (Diffraction Integration Advanced Light Sources, [49]) and xia2 [50] and the results are curated and displayed in ISPyB [47] and SynchWeb [51]. Overall, the software provides automated data collection and processing with minimal user intervention, and allows the full remote operation of the beamline.

A typical example of more complex experimental data is available online [52]. This data, from 3,5-dinitrobenzoic acid (3,5-DNBA) C2/c polymorph [53], recorded during in house research (DLS proposal: NR18193), consists of a 180° φ scan at $2\theta = 0°$ degrees, three 170° ω scans at $2\theta = 30°$ ($\varphi = 0°$, 120°, 240°) then a 180° φ scan and three 170° ω scans at $2\theta = 55°$ to give data to 0.48 Å (Table 2). The first four scans in this series are used for a typical full-sphere data collection to 0.58 Å resolution at 0.6889 Å.

Table 2. Crystallographic data for 3,5-dinitrobenzoic acid (3,5-DNBA).

Data Parameter	Suggested	Low	High
High resolution limit	0.48	1.29	0.48
Low resolution limit	9.52	9.53	0.48
Completeness	100.0	100.0	94.5
Multiplicity	5.7	10.9	2.5
I/σ(I)	19.3	48.9	6.4
Rmerge(I)	0.036	0.028	0.100
Rmeas(I)	0.038	0.029	0.122
Rpim(I)	0.013	0.009	0.069
CC half	1.000	1.000	0.992
Total observations	45,334	4812	1000
Total unique	8016	440	397
Space group	C2/c		
Unit cell (Å, °)	a = 20.26353(8), b = 8.75749(2), c = 9.66975(3), α = 90, β = 109.9413(3), γ = 90		

Data processing can also be carried out using the commercial packages CrysAlisPro (Rigaku Oxford Diffraction CrysAlisPro, Rigaku Europe, Unit B6, Chaucer Business Park, Watery Lane, Kemsing Sevenoaks, Kent, UK) or APEX (Bruker AXS, APEX-II, Bruker AXS GmbH, Oestliche Rheinbrueckenstr. 49, Karlsruhe, Germany). For CrysAlisPro, the diffraction images can be read directly using a subroutine within the software package, while for APEX the images need to be converted to the Bruker format. The conversion software was written by Johnson et al. [1] and is available to users of I19.

6. Conclusions

A novel dual air-bearing fixed-χ diffractometer has been developed for Beamline I19 at Diamond Light Source, which allows the rapid collection of multi-scan small-molecule crystallography data sets in shutterless mode. In conjunction with its fully integrated robotic sample changer, it can be operated via remote access with users required only to ship their samples to Diamond, rather than attending the facility themselves. This new mode of operation will allow users to have shorter and more regular

allocations of beamtime, without the inconvenience of travel, and make the operation of the beamline more responsive to more urgent user access.

Selected scientific highlights from Beamline I19 at Diamond Light Source can be found at [54]. The list of user publications supported by the beamline can be found at [55]. Those interested in applying for beamtime at Diamond Light Source can find information on the applications process in the user web pages [56].

Author Contributions: D.R.A. provided the original concept for the new diffractometer design and also managed the development project. H.N. managed the robot BART upgrade project for the new end-station, with the assistance of S.A.B. and M.R.W., and wrote the BART section of the paper. S.A.B. assisted M.T.H. with the key details of much of the design work and they both provided the majority of the figures for the paper. S.A.B. also assisted with the drafting of the paper. M.R.W. worked out the details of the dynamic sphere-of-confusion correction and this was implemented in EPICS by T.B. and A.J.F. A.W. was responsible for the assembly of both the diffractometer and robot mechanical components. S.A.B., H.N., M.R.W., J.C. and L.K.S. undertook numerous diffraction studies with the new instrument during the commissioning-with-X-rays phase. A.P. was lead mechanical engineer on the project and, along with M.T.H. and L.Z., supervised the design. S.P. and L.C. were responsible for the electrical design while R.M. and S.T. carried out the wiring of the instrument. A.F. and T.B. commissioned the operation and controls of the motion hardware. S.L. and M.A.W. provided assistance with the development of the hardware and controls of the BART robot. P.V.H. developed the GDA software for the high-level control and operation of the complete system with the assistance of M.G. G.W. and M.G. developed software for sample screening and post processing following data collection. R.W.W. is the managing director of Fluid Film devices and was responsible for the design and manufacture of the air-bearings including the final assembly of the goniometer.

Conflicts of Interest: The authors declare no conflicts of interest.

References and Notes

1. Johnson, N.T.; Waddell, P.G.; Clegg, W.; Probert, M.R. Remote Access Revolution: Chemical crystallographers enter a new era at Diamond Light Source beamline I19. *Crystals* **2017**, submitted.
2. Dectris AG. Available online: https://www.dectris.com/ (accessed on 5 October 2017).
3. Bruker AXS Ltd. Available online: https://www.bruker.com/products/x-ray-diffraction-and-elemental-analysis/single-crystal-x-ray-diffraction.html (accessed on 5 October 2017).
4. Nowell, H.; Barnett, S.A.; Christensen, K.E.; Teat, S.J.; Allan, D.R. I19, the small-molecule single-crystal diffraction beamline at Diamond Light Source. *J. Synchrotron Radiat.* **2012**, *19*, 435–441. [CrossRef] [PubMed]
5. Allan, D.R.; Collins, S.P.; Evans, G.; Hall, D.; McAuley, K.; Owen, R.L.; Sorensen, T.; Tang, C.C.; von Delft, F.; Wagner, A.; et al. Status of the crystallography beamlines at Diamond Light Source. *Eur. Phys. J. Plus* **2015**, *130*, 56. [CrossRef]
6. Barnett, S.A.; Nowell, H.; Warren, M.; Wilcox, A.; Allan, D.R. Facilities for small-molecule crystallography at synchrotron sources. *Protein Pept. Lett.* **2016**, *23*, 211–216. [CrossRef] [PubMed]
7. Pflugrath, J.W. The finer things in X-ray diffraction data collection. *Acta Crystallogr. D Biol. Crystallogr.* **1999**, *55*, 1718–1725. [CrossRef] [PubMed]
8. He, B.B. 5.1.3 Sample Stages. In *Two-Dimensional X-ray Diffraction*; John Wiley and Sons Inc.: Hoboken, NJ, USA, 2009; ISBN 978-1-118-21075-8.
9. Helliwell, J.R. Section 2.2.6. Diffractometry. In *International Tables for Crystallography*, 3rd ed.; Prince, E., Ed.; Kluwer Academic Publishers: Dordrecht, The Netherlands, 2006; pp. 36–37. ISBN 978-1-4020-1900-5.
10. International Organization for Standardization, ISO 492:2014. Available online: www.iso.org (accessed on 14 September 2017).
11. HUBER Diffraktionstechnik GmbH & Co. KG. Available online: http://www.xhuber.de/en/product-groups/1-positioning-devices/12-rotation/1-circle-goniometers/480/ (accessed on 21 September 2017).

12. Fluid Film Devices Ltd. Unit 8, Greatbridge Business Park, Budds Lane, Romsey, Hampshire, SO51 0HA, UK. Available online: http://www.fluidfilmdevices.co.uk/static.htm (accessed on 14 September 2017).

13. Powell, J.W. *The Design of Aerostatic Bearings*; The Machinery Publishing Co., Ltd.: Brighton, UK, 1970.

14. ANSYS Workbench Platform, Ozen Engineering Inc., 1210 E Arques Ave #207, Sunnyvale, CA 94085. Available online: www.ozeninc.com/ansys-workbench/ (accessed on 14 September 2017).

15. Acrona Engineering Ltd. Available online: https://www.acrona-engineering.co.uk/ (accessed on 25 September 2017).

16. Heason Technology Ltd. Available online: https://www.heason.com/ (accessed on 14 September 2017).

17. Pandect Precision Components Ltd. Available online: http://www.slipring.co.uk/ (accessed on 14 September 2017).

18. Renishaw. Available online: http://www.renishaw.com/en/1030.aspx (accessed on 14 September 2017).

19. PM-Bearings. Available online: http://www.pm-bearings.nl/ (accessed on 14 September 2017).

20. CA Models. Available online: http://www.camodels.co.uk/ (accessed on 14 September 2017).

21. THK (Toughness High-Quality Know-How). Available online: http://www.thk.com/ (accessed on 14 September 2017).

22. Qioptiq. Available online: http://www.qioptiq.com/ (accessed on 14 September 2017).

23. Agate Products Ltd. Available online: http://agateproducts.co.uk/ (accessed on 20 September 2017).

24. Newport. Available online: https://www.newport.com (accessed on 14 September 2017).

25. Allied Vision. Available online: https://www.alliedvision.com (accessed on 14 September 2017).

26. JJ X-ray. Available online: http://www.jjxray.dk/ (accessed on 14 September 2017).

27. Thorlabs. Available online: https://www.thorlabs.com/ (accessed on 14 September 2017).

28. Parker Motion Control Systems. Available online: https://www.parkermotion.com/ (accessed on 14 September 2017).

29. CRYTUR spol. s r.o., Palackeho 175, 51101 Turnov, Czech Republic. Available online: https://www.crytur.cz/ (accessed on 14 September 2017).

30. Keyence (UK) Ltd. Available online: http://www.keyence.co.uk/ (accessed on 14 September 2017).

31. IMI Precision Engineering, Norgren Ltd. Available online: https://www.imi-precision.com/uk/en/ (accessed on 14 September 2017).

32. Oxford Cryosystems Ltd. Available online: http://www.oxcryo.com/ (accessed on 14 September 2014).

33. Hitachi High-Technologies Science America Inc. Available online: http://www.hitachi-hightech.com (accessed on 14 September 2017).

34. Experimental Physics and Industrial Control System. Available online: http://www.aps.anl.gov/epics/ (accessed on 14 September 2017).

35. Delta Tau Data Systems, Inc. Available online: http://www.deltatau.com (accessed on 14 September 2017).

36. Tapeswitch Ltd. Available online: http://www.tapeswitch.co.uk/ (accessed on 14 September 2017).

37. Cobb, T.; Chernousko, Y.; Uzun, I. I19, Zebra: A flexible solution for controlling scanning experiments. In Proceedings of the ICALEPS2013, San Francisco, CA, USA, 6–11 October 2013; pp. 736–739.

38. BART Robot System, Diamond Light Source. Available online: http://www.diamond.ac.uk/Home/Corporate-Literature/Annual-Review/Review2015/Villages/Macromolecular-Crystallography-Village/Macromolecular-Crystallography-Village-Developments/BART---the-new-robotic-sample-changer-for-MX-beamlines-at-Diamond.html (accessed on 14 September 2017).

39. O'Hea, J.D.; Burt, M.J.; Jones, K.M.; McAuley, K.E.; Preece, G.; Williams, M.A. BART: A sample exchange system for MX Beamlines. In Proceedings of the 16th International Conference on Accelerator and Large Experimental Physics Control Systems. in preparation.

40. Mitsubishi Electric. Available online: http://mitsubishirobotics.com/ (accessed on 14 September 2017).

41. Omron. Available online: https://industrial.omron.co.uk/en/home (accessed on 14 September 2017).

42. Unipuck (The Universal Puck Project). Available online: http://smb.slac.stanford.edu/robosync/Universal_Puck/ (accessed on 14 September 2017).

43. Diamond Light Source Generic Data Acquisition (GDA) Software. Available online: http://www.opengda.org/ (accessed on 14 September 2017).

44. Gibbons, E.P.; Heron, M.T.; Rees, N.P. GDA and EPICS working in unison for science driven data acquisition and control at Diamond Light Source. In Proceedings of the ICALEPCS, Grenoble, France, 10–14 October 2011; pp. 529–532.

45. ISPyB (Information System for Protein crystallographY Beamlines). Available online: http://www. esrf.eu/home/UsersAndScience/Experiments/structural-biology-2/software/ispyb.html (accessed on 14 September 2017).

46. Delageniere, S.; Brenchereau, P.; Launer, L.; Ashton, A.W.; Leal, R.; Veyrier, S.; Gabadinho, J.; Gordon, E.J.; Jones, S.D.; Levik, K.E.; et al. ISPyB: An information management system for synchrotron macromolecular crystallography. *Bioinformatics* **2011**, *27*, 3186–3192. [CrossRef] [PubMed]

47. Kraft, P.; Bergamaschi, A.; Broennimann, C.; Dinapoli, R.; Eikenberry, E.F.; Henrich, B.; Johnson, I.; Mozzanica, A.; Schleputz, C.M.; Willmott, P.R.; et al. Performance of single-photon-counting PILATUS detector modules. *J. Synchrotron Radiat.* **2009**, *16*, 368–375. [CrossRef] [PubMed]

48. Gerstel, M.; Gildea, R.J.; Waterman, D.G.; Ashton, A.W.; Winter, G. Automated Data Processing on the Chemical Crystallography Beamline I19 at Diamond Light Source. 2017; in preparation.

49. Winter, G.; Waterman, D.G.; Parkhurst, J.M.; Brewster, A.S.; Gildea, R.J.; Gerstel, M.; Fuentes-Montero, L.; Vollmar, M.; Michels-Clark, T.; Young, I.D.; et al. DIALS: Implementation and Evaluation of a New Integration Package. 2017; submitted.

50. Winter, G. xia2: An expert system for macromolecular crystallography data reduction. *J. Appl. Cryst.* **2010**, *43*, 186–190. [CrossRef]

51. Fisher, S.J.; Levik, K.E.; Williams, M.A.; Ashton, A.W.; McAuley, K.E. SynchWeb: A modern interface for ISPyB. *J. Appl. Cryst.* **2015**, *48*, 927–932. [CrossRef] [PubMed]

52. The example data set can be found at https://zenodo.org/record/1036416 (accessed on 30 October 2017).

53. Prince, P.; Froncek, F.R.; Gandour, R.D. Two polymorphs of 3,5-dinitrobenzoic acid. *Acta Cryst. C* **1991**, *47*, 895–898. [CrossRef]

54. The Science Highlights Web Page of Beamline I19 at Diamond Light Source. Available online: http://www. diamond.ac.uk/Beamlines/Materials/I19/highlights.html (accessed on 31 October 2017).

55. The User Publications Web Page of Beamline I19 at Diamond Light Source. Available online: http://www. diamond.ac.uk/Beamlines/Materials/I19/publications.html (accessed on 31 October 2017).

56. The User Access Web Pages of Diamond Light Source. Available online: http://www.diamond.ac.uk/Users. html (accessed on 31 October 2017).